Electronic Supplementary Material (ESI) for Journal of Materials Chemistry A.
This journal is © The Royal Society of Chemistry 2020

Electronic Supplementary Information

Immobilizing single atom catalytic sites onto highly reduced carbon hosts: Fe–N_4/CNT as a durable oxygen reduction catalyst for Na-air battery

Woo Yeong Noh,[a] Eun Mi Kim,[b] Kwang Young Kim,[a] Jin Hyun Kim,[a] Hu Young Jeong,[c] Pankaj Sharma,[a] Geunsik Lee,[b] Ji-Wook Jang,*[a] Sang Hoon Joo,*[a,b] Jae Sung Lee*[a,d]

[a]School of Energy and Chemical Engineering, Ulsan National Institute of Science and Technology (UNIST), 50 UNIST-gil, Ulsan 44919, Republic of Korea

[b]Department of Chemistry, Ulsan National Institute of Science and Technology (UNIST), Ulsan 44919, Republic of Korea

[c]UNIST Central Research Facilities, Ulsan National Institute of Science and Technology (UNIST), 50 UNIST-gil, Ulsan 44919, Republic of Korea

[d]Department of Energy Engineering, Ulsan National Institute of Science and Technology (UNIST), Ulsan 44919, Republic of Korea

Corresponding Authors

E-mail: jlee1234@unist.ac.kr (J. S. L.); shjoo@unist.ac.kr (S. H. J.); jiwjang@unist.ac.kr (J.-W. J.)

Table of Contents

1. Experimental Details

Synthesis of microwave-annealed Fe–N_4 on CNT (MA-Fe-N/CNT). Multi-walled carbon nanotubes (CNTs, Hanwha Nanotech) were refined in 1 M HCl at 60 °C for 1 day and oxidized with an acid mixture (nitric acid (69 %) + concentrated sulfuric acid (90 %) with a volumetric ratio of 1:3) at 60 °C for 3 h. The oxidized CNTs (Ox-CNTs) were filtered by an ample amount of de-ionized (DI) water, dialyzed in a 0.1 % Triton X-100 solution for 3 days, and lyophilized. In the synthesis of the ternary FePc/CNT@Mel composites, 160 mg of Ox-CNTs and 160 mg of iron(II) phthalocyanine (FePc, Sigma-Aldrich) were first mixed and sonicated in water. The FePc-adsorbed CNTs were prepared by a hydrothermal reaction at 180 °C for 12 h and freeze-dried for 1 day. The ternary FePc/CNT@Mel composites were then prepared by ultrasonically blending melamine (Mel, 600 mg) and a FePc-adsorbed CNT (120 mg) suspension in 10.0 mL of ethanol. They were dried in an oven at 60 °C for 8 h to remove the remaining moisture and then transferred into the crucible purged with argon (Ar) gas for more than 30 minutes to make an inert atmosphere. The crucible was immediately moved into a household microwave (B821118215, Winiadaewoo, 2.45 GHz, 1.0 kW) and microwaved for just 4 min. We controlled the ratio of FePc to Ox-CNTs and the irradiation time to optimize the microwave annealing conditions. The best-activity catalyst was obtained with a 1:1 ratio using an irradiation time of 4 min. The resulting powder was ground in a mortar and etched in 0.5 M H_2SO_4 at 80 °C for 8 h. After filtering with deionized water several times, the samples were dried at 70 °C in a vacuum oven overnight to obtain MA-Fe-N/CNT samples.

Synthesis of thermally annealed Fe–N_4 on a CNT (TA-Fe-N/CNT). The TA-Fe-N/CNT samples were prepared identically except for using conventional thermal annealing instead of microwave annealing. The ternary FePc/CNT@Mel composites were heated to 900 °C under an Ar atmosphere for 2 h with a ramping rate of 5 °C min^{-1} and a flow rate of 100 mL min^{-1}. In the same manner, the resulting powder was ground in a mortar and etched in 0.5 M H_2SO_4 at 80 °C for 8 h. After filtering with deionized water several times, the samples were dried at 70 °C in a vacuum oven overnight.

Physical characterization. The atomic-resolution HRTEM, HAADF-STEM images, and EELS spectrum of the samples were taken using a double-side spherical aberration-corrected transmission electron microscope (TEM, Titan3 G2 cube 60-300, FEI Company, Netherlands) under an accelerating voltage of 80 and 200 keV. Raman spectroscopy (WITec alpha300R, 532 nm laser) was used to study the structure and disorder of the catalysts. X-ray photoelectron spectroscopy (XPS) measurements were performed on an ESCLAB 250Xi (Thermo Scientific) using an Al K_α X-ray source monochromatic operating at 1486.6 eV.

Synchrotron XAS measurements. Synchrotron X-ray absorption spectroscopy (XAS) measurements were conducted at the beamline 7D of Pohang Accelerator Laboratory (PLS-II, 3.0 GeV) in Pohang, Korea. The radiation was monochromatized using a Si (111) double crystal monochromator and the incident beam was detuned by 15 % to minimize high-order harmonics. The spectra for Fe *K*-edge were obtained in transmission detection mode at room temperature. The intensity of the incident beam was monitored using a He-filled IC Spec ionization chamber. The spectra for Fe *K*-edge were obtained in transmission detection mode at room temperature. For each sample, the reference spectrum of Fe foil was taken simultaneously so that the energy in the spectrum of sample could be calibrated with respect to the *K*-edge energy of Fe metal. The ATHENA and ARTEMIS in the IFEFFIT suite of software programs were used to analyze the obtained data to study the local structure of Fe in the as-prepared catalysts. EXAFS spectra were fitted using the FEEF 9.0 code and the structure parameters obtained from the DFT calculations.

CO pulse chemisorption and TPD. Pulse chemisorption and TPD measurements of CO were performed on a BELCAT-II (MicrotracBEL) under a 30 mL min^{-1} He flow as carrier gas. For each catalyst, an amount of 100 mg was mounted between quartz wool in a reactor assembling in a furnace. All samples were thermally pre-treated up to 300 K with a ramp of 10 ˚C min^{-1} in inert He gas to remove any possible surface contamination. Pulse chemisorption was carried out at -80 ˚C using a CATCryo-II (MicrotacBEL). Five consecutive 0.947 mL CO were injected at an interval of 25 min, and its uptake per mole was monitored and quantified using a thermal conductivity detector (TCD). In TPD experiments, the sample powder was purged by 10 vol.% CO/He and heated up to 450 K with 10 C min^{-1} ramping rate while recording the TCD signal of outlet gases. Assuming that each catalytic active site is blocked by one CO molecule, the molar amount of adsorbed CO per $g_{catalys}$t n_{CO} (in mol g^{-1}) is equal to the molar concentration of active surface sites. By multiplying the measured values with Avogadro's constant N_A, we can get the mass-based surface site density (MSD).

Electrochemical characterization. Electrochemical tests toward ORR were performed *via* the RDE and RRDE techniques in a standard three-electrode cell using a potentiostat (Ivium Stat.h, Ivium Technologies), an RDE (AFE3T050GC, Pine Research; disk geometric area 0.196 cm^2), and an RRDE (AFE7R9GCPT, Pine Research; disk geometric area 0.247 cm^2). Potentials were measured *vs.* Hg/HgO (RE-61AP, ALS; 1 M NaOH filling solution) and Ag/AgCl (RE-1B, ALS; 3.0 M NaCl filling solution) reference electrodes in alkaline and acid electrolytes, respectively, and then converted to the reversible hydrogen electrode (RHE) scale by calibration. The RHE calibration values were established by the thermodynamic potential for the H^+/H_2 reaction which was measured in a H_2-saturated electrolyte with platinum wire as the working electrode. All measurements were performed using a graphite rod as the counter electrode to avoid any contamination by platinum (Pt). To prepare the catalyst ink, 10 mg of the catalyst was ultrasonically mixed for 30 min with 20 µl of a 5 wt% Nafion solution (Aldrich), 65 µl of water, and 425 µl of ethanol. From this homogeneous catalyst ink, 10.3 µl was deposited onto the disk, resulting in an approximate loading of 0.8 mg cm^{-2} (or, 0.6, 0.4 and 0.2 mg cm^{-2}). The Pt/C catalyst (Johnson-Matthey, 20 wt% Pt) with geometric Pt loading of 50 μg_{pt} cm^{-2} was used as the benchmark. The electrolytes were oxygen (O_2)-saturated 0.1 M KOH (99.99% Samchun) and 0.1 M $HClO_4$ (70%, GFS Chemicals). Prior to every measurement, the RDE or RRDE were polished with a 1.0 µm alumina suspension and then with an ethanol, and the glass cell was leached with 0.5 M H_2SO_4 solution. Each catalyst was activated by 20 cyclic voltammetry (CV) scans at a scan rate of 20 mV s^{-1} in a N_2-saturated electrolyte and a potential range of 0.0–1.3 V_{RHE}. Then, linear sweep voltammetry (LSV) for oxygen reduction reaction (ORR) was performed with a scan rate of 5 mV s^{-1} at 1600 rpm from 1.3 to 0.0 V_{RHE} in the O_2-saturated electrolyte. All currents were corrected for the capacitive current measured in the N_2-saturated electrolyte, and all potentials were iR-corrected by electrochemical impedance spectra measured at 0.68 V_{RHE} with a potential amplitude of 10 mV from 10,000 to 1 Hz. The percentage of H_2O_2 was determined at a ring potential of 1.3 V_{RHE} in the RRDE measurements.

The collection efficiency was 37 %, as calculated using an $Fe(CN)_6^{4-/3-}$ redox couple. Stability tests were performed in the potential range of 0.6–1.0 V_{RHE} in the N_2-saturated electrolyte at a scan rate of 100 mV s^{-1}. In order to avoid the replenishing effect derived from Fe impurities that might be formed during the potential cycling, LSV for ORR after 10,000 cycles was conducted with fully polishing the glass cell and electrolytes.

Density functional theory (DFT) Calculations. The calculations have been performed by using the DFT method as implemented in Vienna *ab initio* simulation package (VASP) code.[55] The plane wave energy cutoff of 400 eV was used with Perdew–Burke–Ernzerhof (PBE) parameterization of the general gradient approximation exchange-correlation functional[56]. Spin polarization has been included for all the calculations. For proper description of Fe d electron correlation energy, the Hubbard-U = 5.0 eV has been considered. The slab model with in-plane lattice parameters a = 17.22 Å, b = 12.78 Å are used with a sufficient vacuum region 20 Å along the perpendicular direction. With the k-mesh 1x1x1, all the atomic positions are optimized until the force is less than 0.02 eV/Å with including the van der Waals correction by Grimme's method (D3).[57] For the density of states analysis, the k-mesh 9x12x1 is used. For each step, the Gibbs free energy change is defined as $\Delta G = \Delta E^{DFT} + \Delta ZPE - T\Delta S + \Delta G_U + \Delta G_{pH}$[58], where ΔE^{DFT} is the reaction energy from the reactant to the product (*OOH, *O, *OH) adsorbed on the catalyst surface using the method proposed by Norskov et al.[59] Zero-point energy(ΔZPE) and vibrational entropy $(T\Delta S)$ are obtained from the calculations of the vibrational frequencies of each adsorbed intermediate on the fixed slab model. For the dependency on the pH environment and electrode potential, we applied $\Delta G_{pH} =- k_B T ln[H^+]$ and $\Delta G_U =- eU$ on the total Gipps free energy (ΔG), where U is the electrode potential.

Preparation of cell components of Na-air battery. Carbon felts (XF30A, Toyobo) were used as the air-cathodes for the Na-air batteries. A Na-air battery kit was purchased from 421Energy Co., Ltd. Na metal attached to the surface of a nickel (Ni) mesh was inserted into a pouch cell for use as the anode. An organic non-aqueous liquid electrolyte consisting of 1 M $NaCF_3SO_3$ in tetraethylene glycol dimethyl ether was purchased from Sigma-Aldrich. A Na super ionic conducting (NASICON) membrane with a thickness of 1 mm and an exposed area of 2 cm^2 was used to separate the anode from the cathode. The ionic conductivity of the NASICON discs was measured to be around 1×10^{-3} S cm^{-1} at room temperature. An aqueous liquid electrolyte of 0.1 M NaOH (99.99%) was purchased from Samchun.

The air cathode was prepared by impregnating catalyst slurries (90 wt% catalyst, 10 wt% poly(vinylidene) fluoride (PVDF) binder in N-methyl-2-pyrrolidone (NMP) solvent) onto one side of the carbon felt. The area of the air electrode was 1.0 cm^2, and the mass loading of the catalyst layer was 2.15 mg cm^{-2}. For comparison, Pt/C (Johnson-Matthey, 20 wt% Pt) and TA-Fe-N/CNT were also used as catalysts, and the same loading levels were applied.

Na-air battery assembly and testing. Pouch-type cells were assembled for the Na-air batteries with 0.1 M NaOH aqueous solution. The anode compartment was first assembled by mounting the NASICON disc on the open-structured top part of the anode and then was sealed with the bottom part of the anode, where a Ni tap current collector (Solbrain LTK) with Na metal attached and an organic electrolyte were inserted. Assembly was performed in a glove box under a high-purity Ar atmosphere (O_2 and H_2O < 1 ppm). The anode compartment and air-cathode were mounted in a Na-air battery test cell body with an open-structured cathode, where the air-cathode was immersed in 0.1 M NaOH aqueous solution. The assembled Na-air battery was mildly stirred and connected to a testing station. A potentiostat (Ivium Stat.h, Ivium Technologies) was employed to apply discharge–charge voltage behaviour at the desired current rates.

2. Supporting Figures and Tables

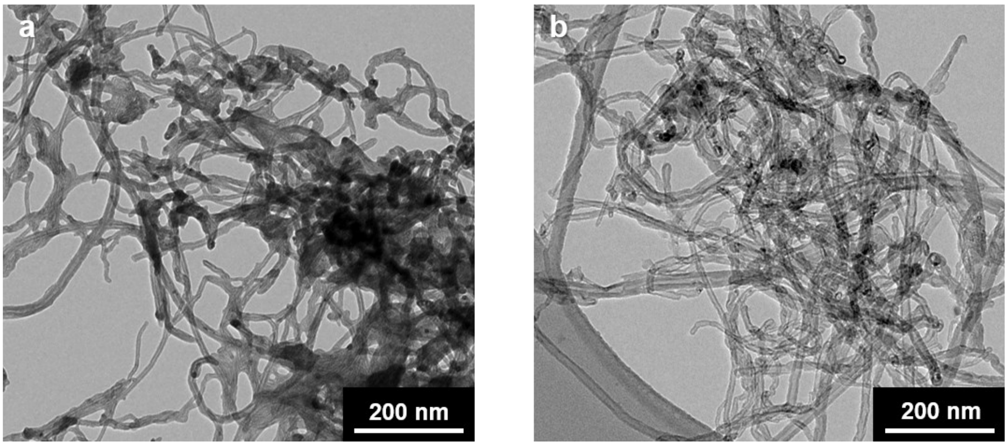

Fig. S1. Structural discrepancy of the carbon supports between MA-Fe-N/CNT and TA-Fe-N/CNT catalysts. HRTEM images of (a) MA-Fe-N/CNT showing thin carbon layers on the CNT surface and (b) TA-Fe-N/CNT catalysts showing thick carbon layers on the CNT surface.

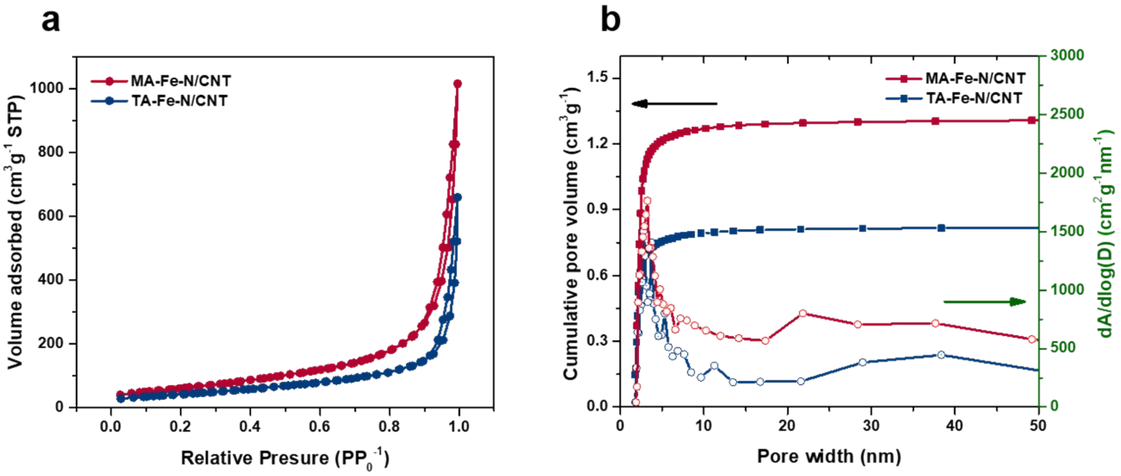

Fig. S2. Pore structure. **(**a) N_2 adsorption-desorption isotherm and (b) Barrett-Joyner-Halenda (BJH) pore size distributions of MA-Fe-N/CNT and TA-Fe-N/CNT catalysts.

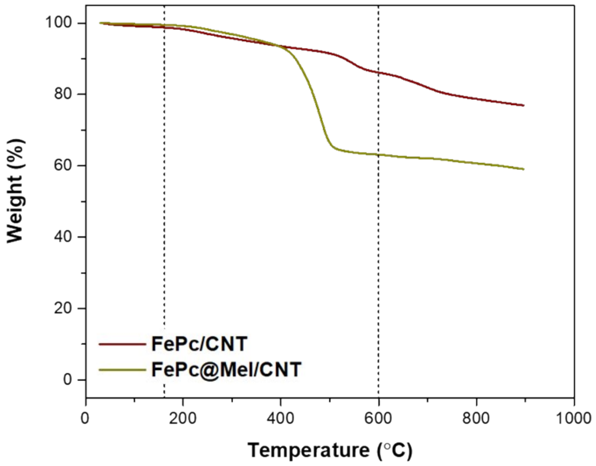

Fig. S3. Thermogravimetric analysis (TGA) of FePc/CNT and FePc@Mel/CNT.

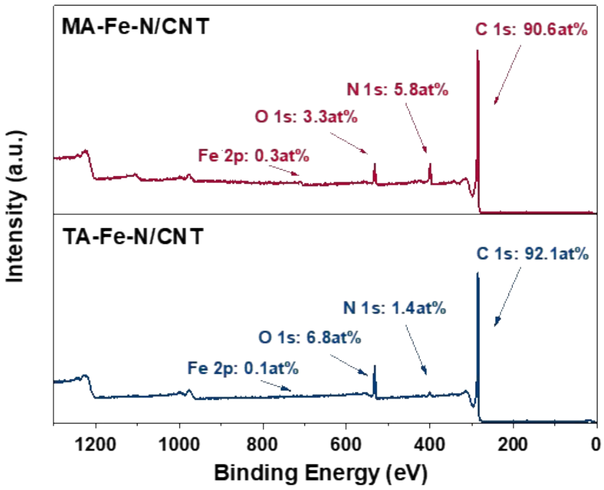

Fig. S4. Wide-scan XPS spectra of MA-Fe-N/CNT and TA-Fe-N/CNT catalysts. The surficial O content of the MA-Fe-N/CNT catalyst (3.3 at%) is much less than that of the TA-Fe-N/CNT catalyst (6.8 at%), indicating that the microwave annealing method could effectively remove O defects.

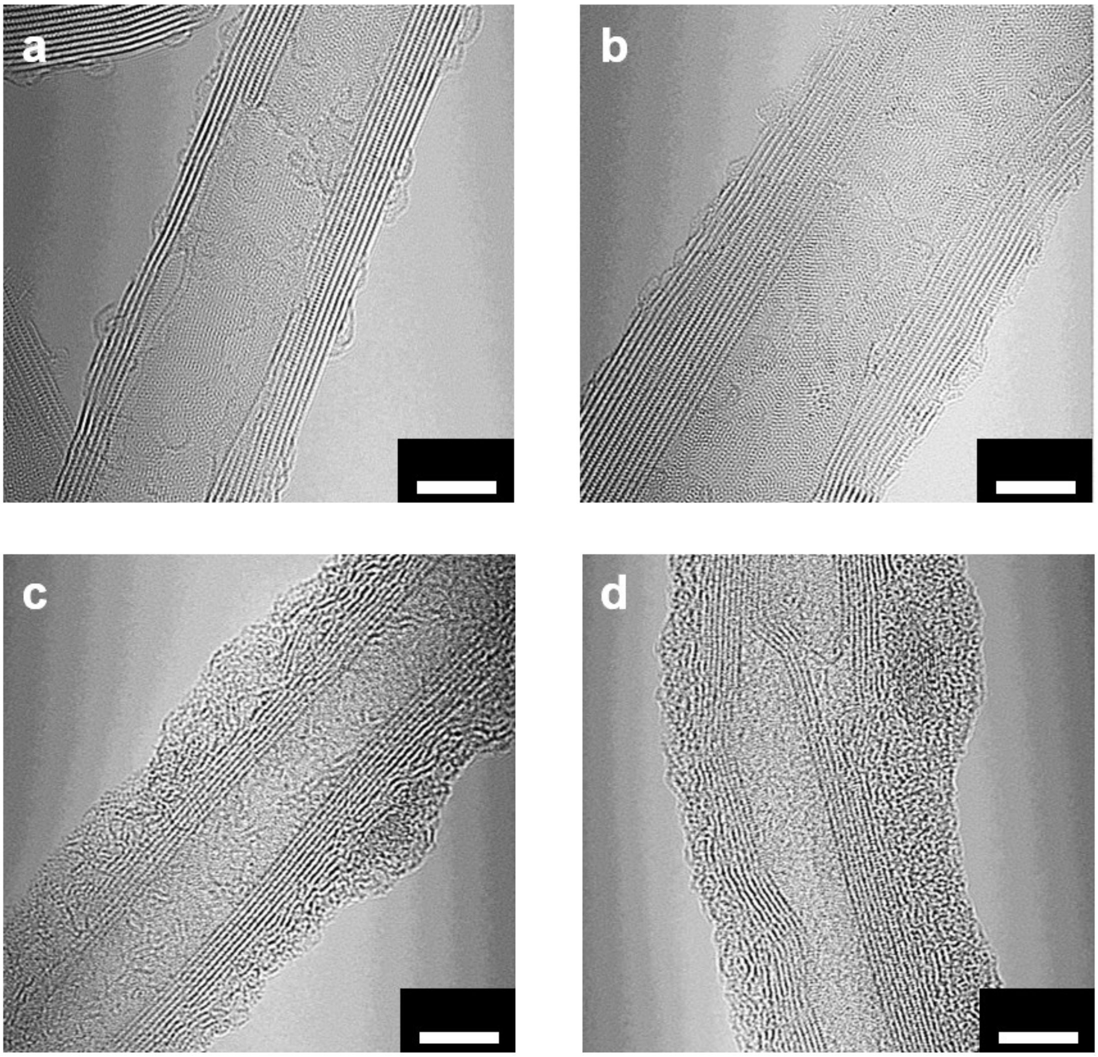

Fig. S5. Atomic-resolution HRTEM images of MA-Fe-N/CNT and TA-Fe-N/CNT catalysts. (a,b) Additional images showing the highly crystallized and thin carbon layers on the CNT surface in the MA-Fe-N/CNT catalyst. (c,d) Additional images showing the amorphous and thick carbon layers on the CNT surface in the TA-Fe-N/CNT catalyst. Scale bars, 5 nm.

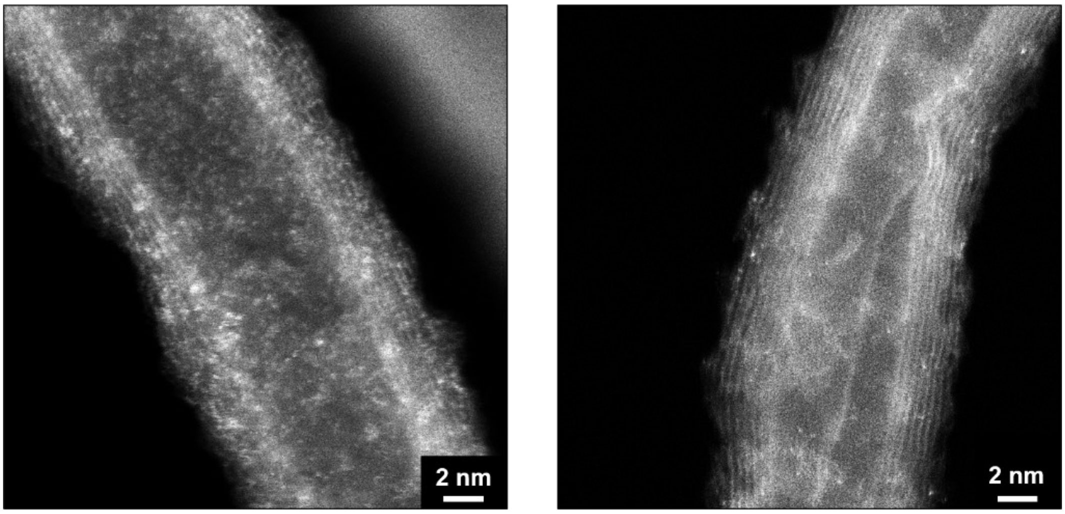

Fig. S6. HAADF-STEM images of MA-Fe-N/CNT catalysts. Additional images showing that a relatively higher proportion of single Fe atoms is distributed on the CNT surface in the MA-Fe-N/CNT catalyst.

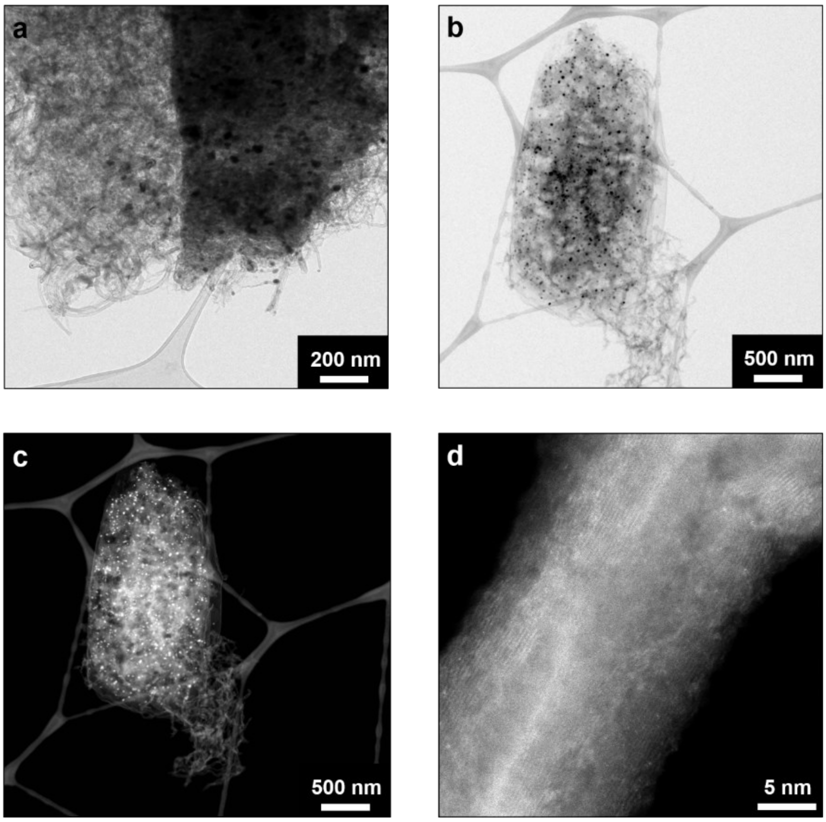

Fig. S7. BFTEM and HAADF-STEM images of TA-Fe-N/CNT catalyst. (a,b) BFTEM and (c,d) STEM images showing that abundant Fe or Fe_3C particles are formed instead of single Fe atoms in the TA-Fe-N/CNT catalyst.

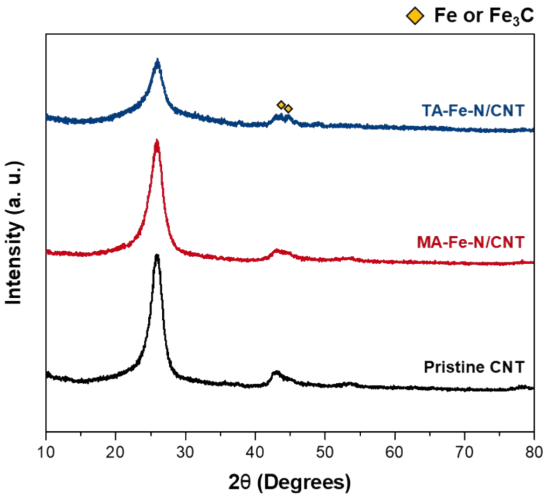

Fig. S8. XRD patterns of MA-Fe-N/CNT and TA-Fe-N/CNT catalysts.

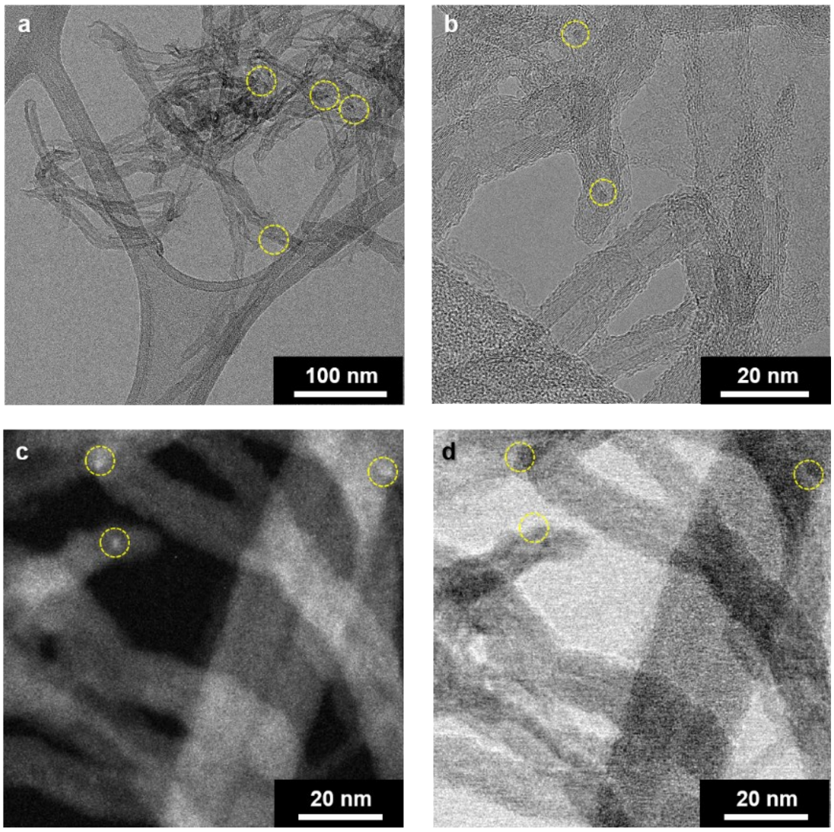

Fig. S9. HRTEM and HRSTEM images of MA-Fe-N/CNT. (a,b) HRTEM and (c,d) HRSTEM images showing that some Fe clusters are formed in MA-Fe-N/CNT.

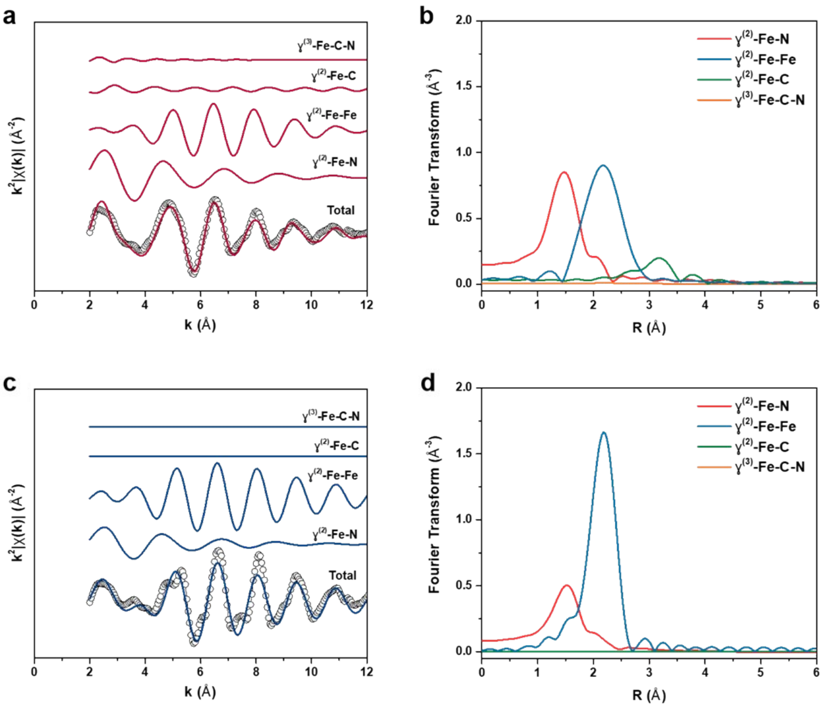

Fig. S10. Fe *K*-edge EXAFS analysis of (top) MA-Fe-N/CNT and (bottom) TA-Fe-N/CNT catalysts. (a) k-spaces and (b) R-spaces fitting curves of MA-Fe-N/CNT. (c) k-spaces and (d) R-spaces fitting curves of TA-Fe-N/CNT. In k-spaces, fitting curves from bottom to top: Fe-N, Fe-Fe and Fe-C $\gamma^{(2)}$ two-body signals and Fe-C-N $\gamma^{(3)}$ three-body signal are included in the fits. No phase-shift correction was applied to the Fourier transforms. The fitted EXAFS parameters are reported in Table S2.

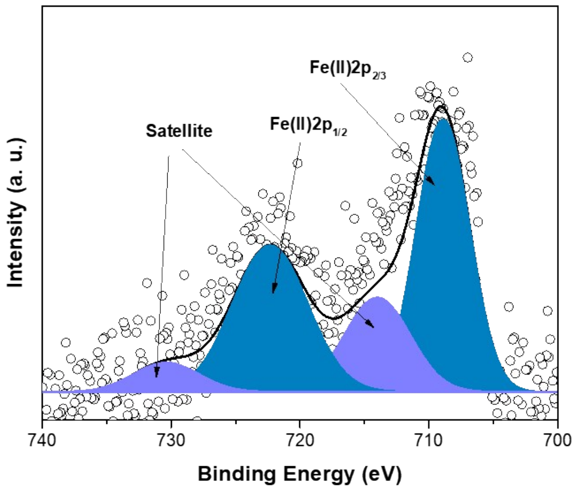

Fig. S11. XPS spectra of Fe2p deconvolution peak of MA-Fe-N/CNT.

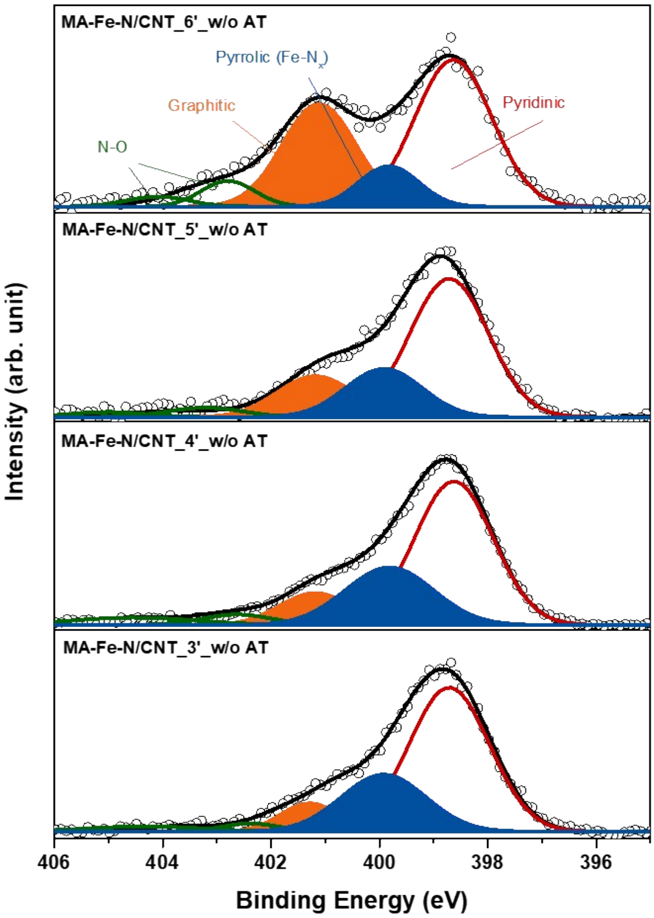

Fig. S12. XPS spectra of N1s deconvolution peak depending on irradiation time. The XPS N1s results indicate the presence of pyridinic-N, pyrrolic-N (Fe-N_x) species, as well as graphitic-N and oxidized N species. The fraction of pyrrolic-N (Fe-N_x) species (blue) gradually decreases while that of graphitic-N (orange) gradually increases with increasing irradiation time.

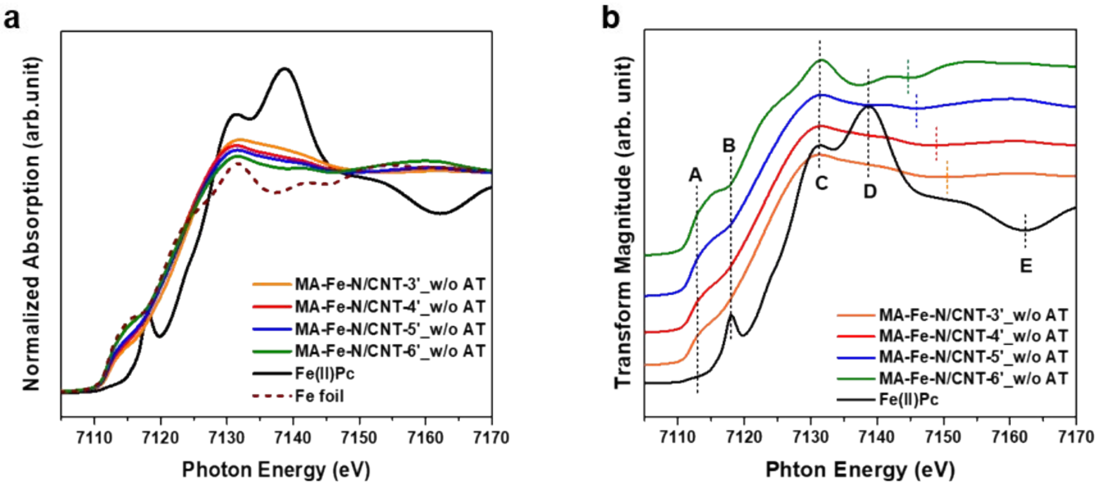

Fig. S13. Fe *K*-edge XANES spectra depending on irradiation time. (a) The intensity of peak A increases, while that of peak C decreases upon increasing the irradiation time in the overlapped spectra. (b) The position of peak E is gradually shifted toward lower energy moment by moment. XANES spectrum of Fe(II)Pc was used as a square-planar Fe^{II}-N_4 standard. Note the changes in the intensities of peaks A and B and the relative position of peak E.

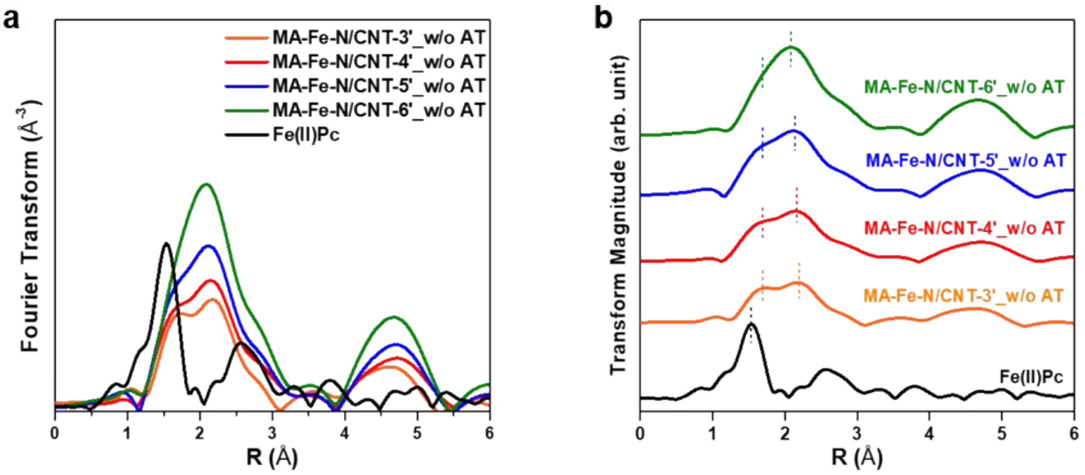

Fig. S14. Fourier-transformed k^3-weighted Fe K-edge EXAFS spectra depending on irradiation time. (a) Progressive enhancement of the peak intensity for Fe-Fe (2.20 Å) over time is evident. (b) All FT-EXAFS spectra for the microwave-treated catalysts show slightly elongated Fe-N scattering peaks (1.7 Å). Note the changes in the relative peak position of Fe-N and the relative peak intensity of Fe-Fe. No phase-shift correction was applied to the Fourier transforms.

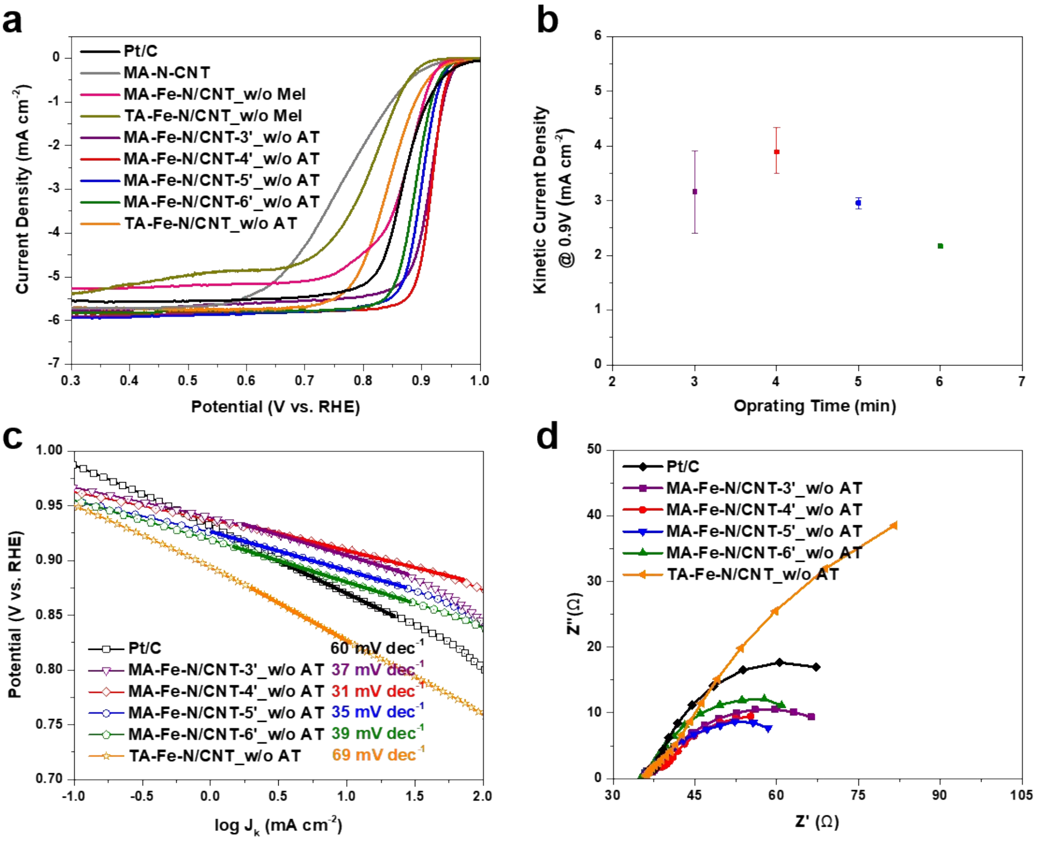

Fig. S15. Comparison of microwave-annealed catalysts for different irradiation times with other control catalysts in alkaline media. (a) RDE curves for various catalysts measured in 0.1 M KOH, (b) comparison of the kinetic current densities at 0.9 V (vs. RHE), (c) Tafel plots, and (d) EIS results.

All measurements were carried out before acid-washing in 0.5 M H_2SO_4. We synthesized the N-doped CNT catalyst (MA-N-CNT) by simply adding melamine to the Ox-CNT, followed by 4 min of microwave irradiation to confirm the effect of introducing Fe-containing moieties. We also prepared MA-Fe-N/CNT-4'_w/o Mel and TA-Fe-N/CNT_w/o Mel catalysts (w/o Mel: without melamine) following the same procedure explained in the "Experimental Methods" section except with the addition of melamine to confirm the effect of introducing a secondary N source. MA-Fe-N/CNT-3', 4', 5'_w/o AT catalysts were measured three times in 0.1 M KOH to confirm the reproducibility and to analyse the trends. The dots indicate the average values, and the error bars were defined using the maximum–minimum range. Linear sweep voltammetry for ORR was performed with a scan rate of 5 mV s^{-1} at 1600 rpm from 1.3 to 0.0 V_{RHE} in the O_2-saturated electrolyte. All currents were corrected for the capacitive current measured in the N_2-saturated electrolyte, and all potentials were iR-corrected. Catalyst loading amount was 0.8 mg cm^{-2} for all measurements (electrode surface area: 0.196 cm^2).

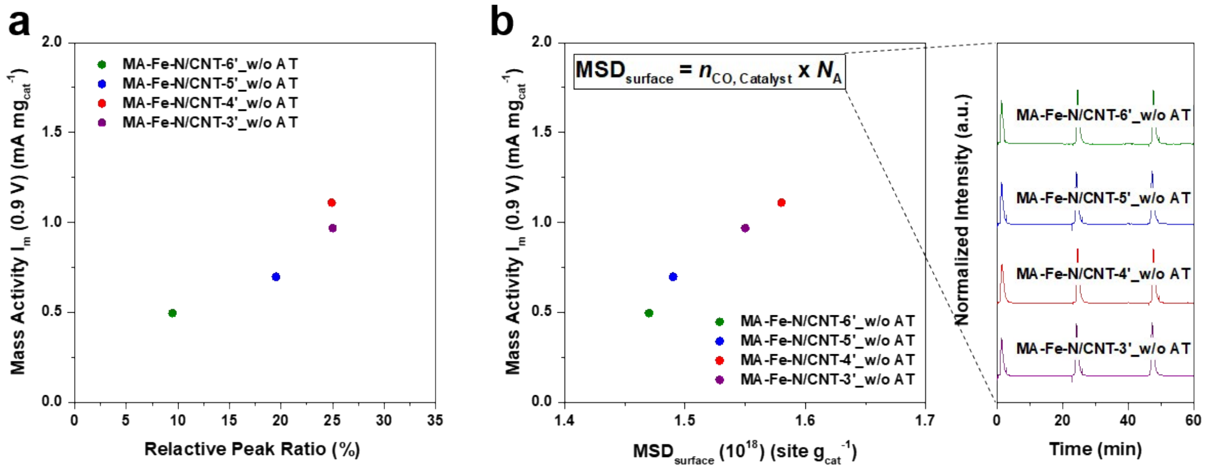

Fig. S16. Correlation of ORR activity and the relative ratio FeN_xC_y moiety. Correlations between the kinetic current densities at 0.9 V (vs. RHE) and the relative quantities of FeN_xC_y moieties obtained from the (a) XPS and (b) CO chemisorption results. A surface mass-based site density (MSD) was calculated from the CO chemisorption results.

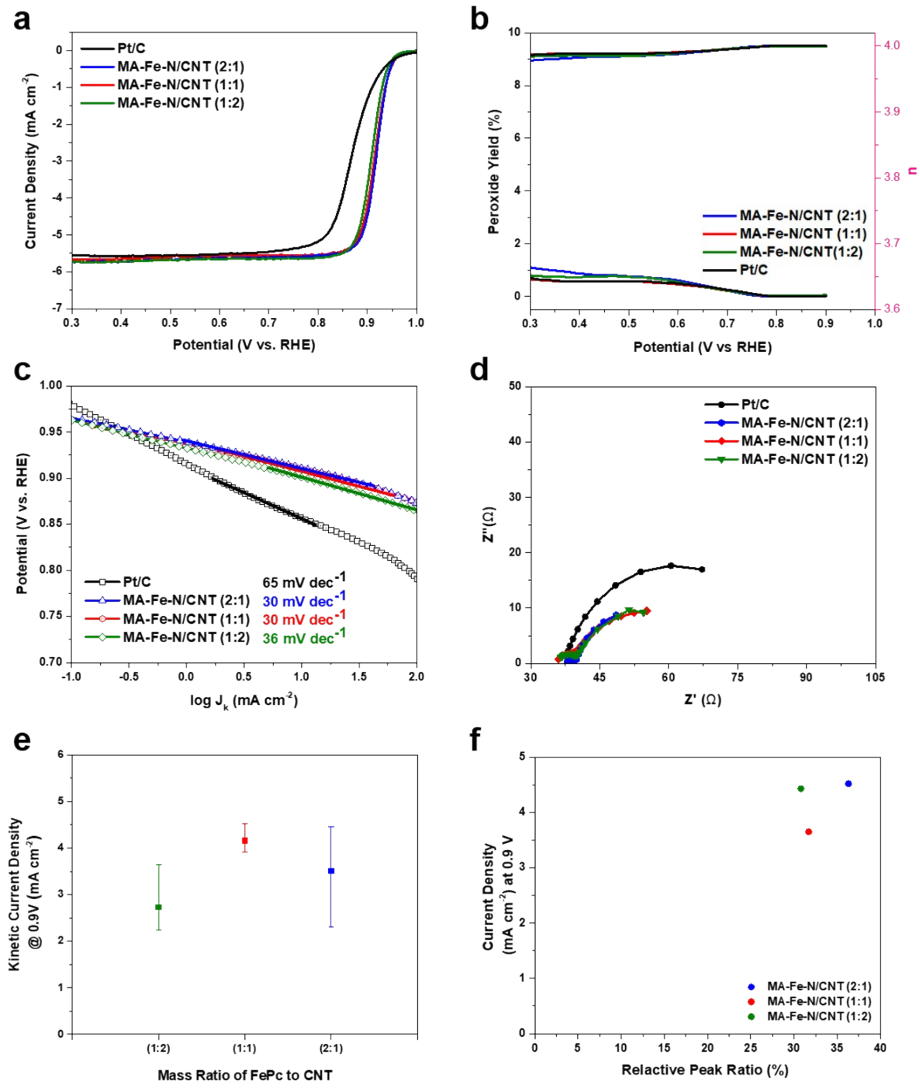

Fig. S17. Microwave-annealed catalysts with different mass ratios of FePc precursor to CNT for ORR in alkaline media. (a) RRDE curves measured in 0.1 M KOH, (b) peroxide yields with electron transfer numbers, (c) Tafel plots, and (d) EIS results. (e) Comparison of the kinetic current density at 0.9 V (*vs*. RHE); all catalysts were measured three times in 0.1 M KOH. The dots indicate the average values, and the error bars were defined using the maximum–minimum range. (f) Correlation of ORR activity and relative ratio FeN_xC_y moiety obtained from XPS. The dots indicate the average values, and the error bars were defined using the maximum–minimum range. Linear sweep voltammetry for ORR was performed with a scan rate of 5 mV s^{-1} at 1600 rpm from 1.3 to 0.0 V_{RHE} in the O_2-saturated electrolyte. All currents were corrected for the capacitive current measured in the N_2-saturated electrolyte, and all potentials were iR-corrected. Catalyst loading amount was 0.8 mg cm^{-2} for all measurements (electrode surface area: 0.247 cm^2).

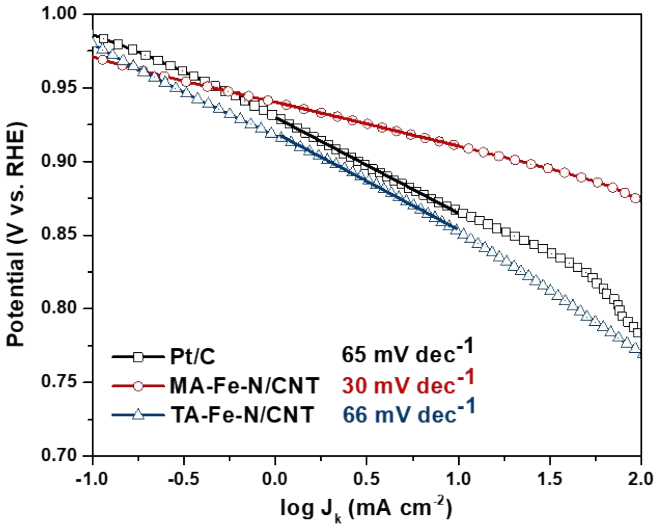

Fig. S18. Tafel plots for MA-Fe-N/CNT, TA-Fe-N/CNT, and Pt/C catalysts in 0.1 M KOH. The order of the Tafel slope (MA-Fe-N/CNT > Pt/C > TA-Fe-N/CNT catalysts was observed.

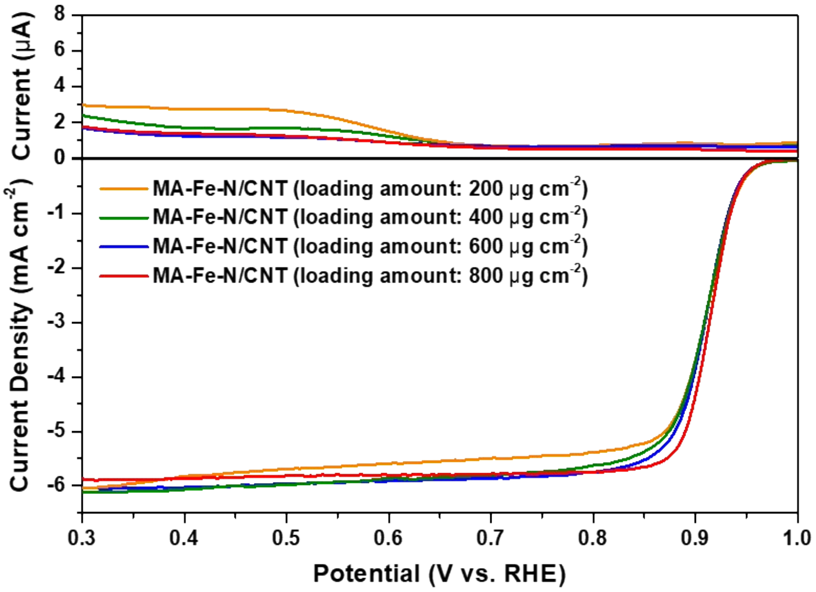

Fig. S19. RRDE polarization curves of MA-Fe-N/CNT catalyst at different loading amounts in 0.1 M KOH. The MA-Fe-N/CNT catalyst shows high ORR activity with high selectivity regardless of the catalyst loading amount.

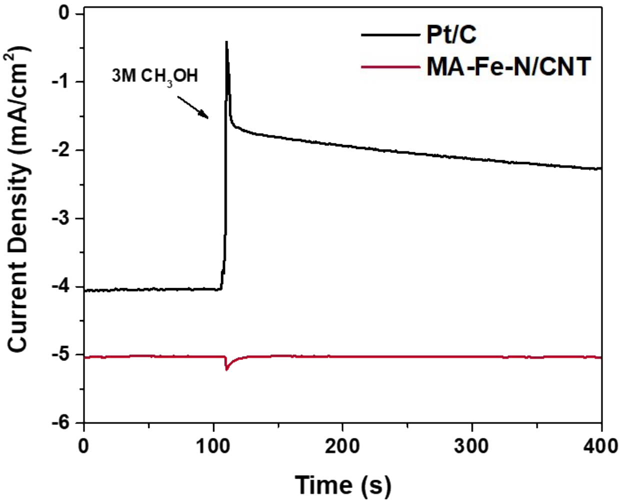

Fig. S20. Chronoamperometric (current-time) responses of Pt/C and MA-Fe-N/CNT for ORR at 0.7 V_{RHE}, followed by the introduction of methanol (3 M) in O_2-saturated 0.1 M KOH at a rotation speed of 1600 rpm. The MA-Fe-N/CNT catalyst shows much better methanol tolerance than Pt/C, with only a negligible change in the current density after the introduction of methanol.

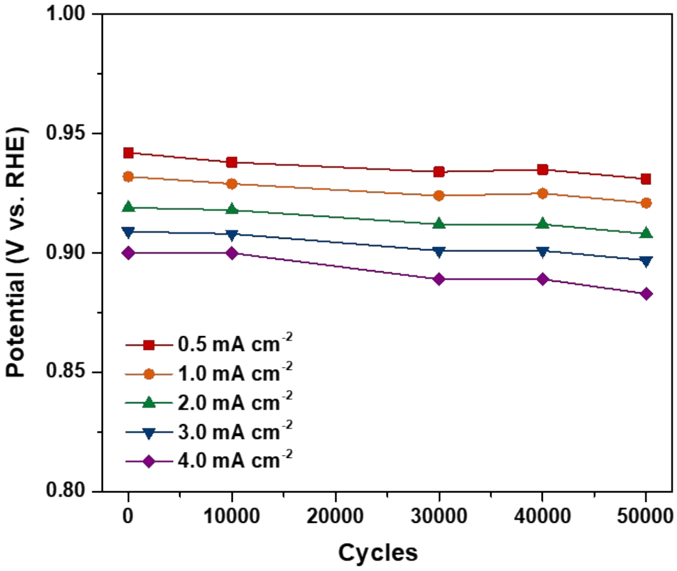

Fig. S21. Long-term durability tests up to 50,000 cycles. Change in potential as a function of cycle number for MA-Fe-N/CNT catalyst.

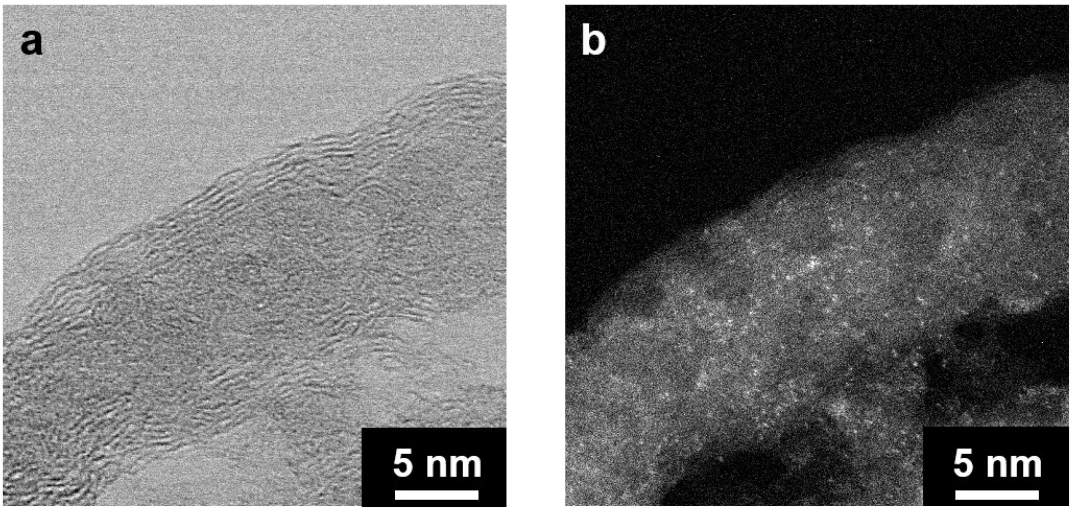

Fig. S22. STEM images of MA-Fe-N/CNT catalyst after 10,000 potential cycles. (a) BFTEM and (b) STEM images show that CNT support and single atomic Fe-N_4 species do not undergo any considerable deterioration.

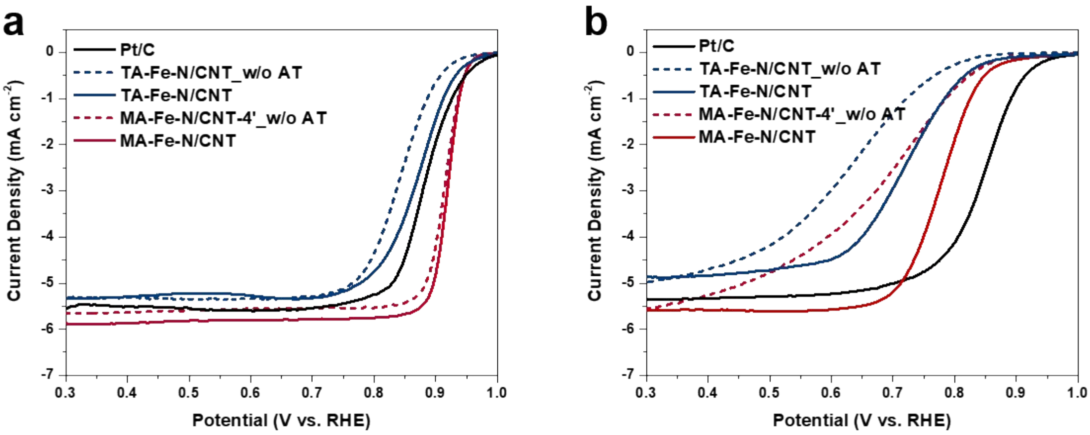

Fig. S23. RDE polarization curves for MA-Fe-N/CNT and TA-Fe-N/CNT catalysts before and after acid treatment in (a) alkaline and (b) acidic media. The effectiveness of SMA and acid treatment seems to be more prominent in the acid electrolytes. Linear sweep voltammetry for ORR was performed with a scan rate of 5 mV s^{-1} at 1600 rpm from 1.3 to 0.0 V_{RHE} in the O_2-saturated electrolyte. All currents were corrected for the capacitive current measured in the N_2-saturated electrolyte, and all potentials were iR-corrected. Catalyst loading amount was 0.8 mg cm^{-2} for all measurements (electrode surface area: 0.196 cm^2).

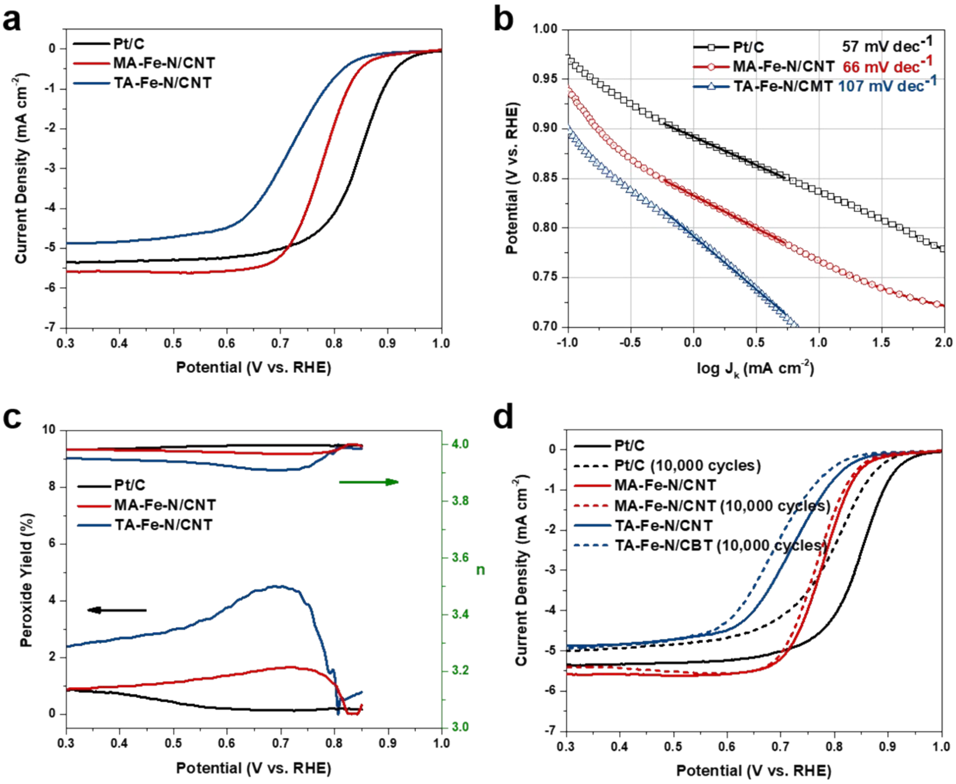

Fig. S24. Electrochemical performance comparison in acid media. (a) RRDE polarization curves of MA-Fe-N/CNT, TA-Fe-N/CNT, and Pt/C in O_2-saturated acid electrolyte. (b) Tafel plots of MA-Fe-N/CNT, TA-Fe-N/CNT, and Pt/C catalysts. (c) Peroxide yield with electron transfer numbers measured *via* RRDE testing. (d) Polarization curves after 10,000 potential cycles in acid media are also given. Conditions: RRDE measurements at room temperature with a rotation rate of 1600 rpm, in 0.1 M $HClO_4$. The stability tests involved 10,000 potential cycles between 0.6 V to 1.0 V (vs. RHE) in the N_2-saturated electrolytes. All currents were corrected for the capacitive current measured in the N_2-saturated electrolyte, and all potentials were iR-corrected. Catalyst loading amount was 0.8 mg cm^{-2} for all measurements (electrode surface area: 0.247 cm^2).

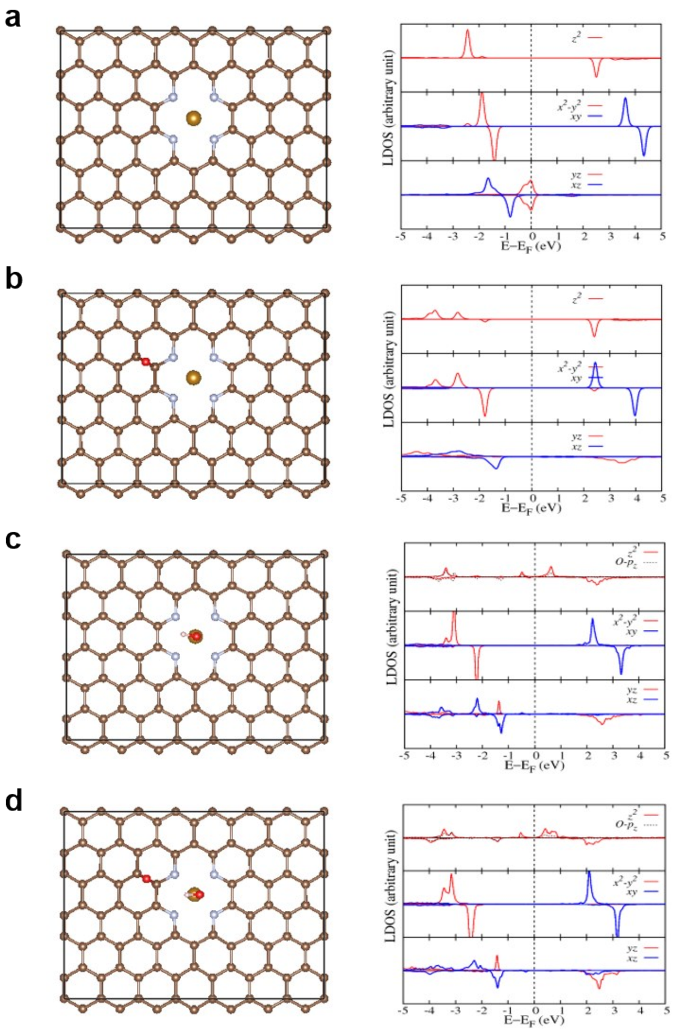

Fig. S25. Projected DOS analysis for clean and Type II Fe–N_4 structures. (a) (left) Clean Fe–N_4 structure, (right) projected DOS of Fe d orbitals. (b) (left) Fe–N_4 with an epoxide (type II), (right) projected DOS of Fe d orbitals. (c) (left) clean Fe–N_4 structure, (right) projected DOS of Fe d orbitals and pz orbital of O. (d) (left) clean Fe–N_4 structure with an epoxide (type II), (right) projected DOS of Fe d orbitals and pz orbital of O.

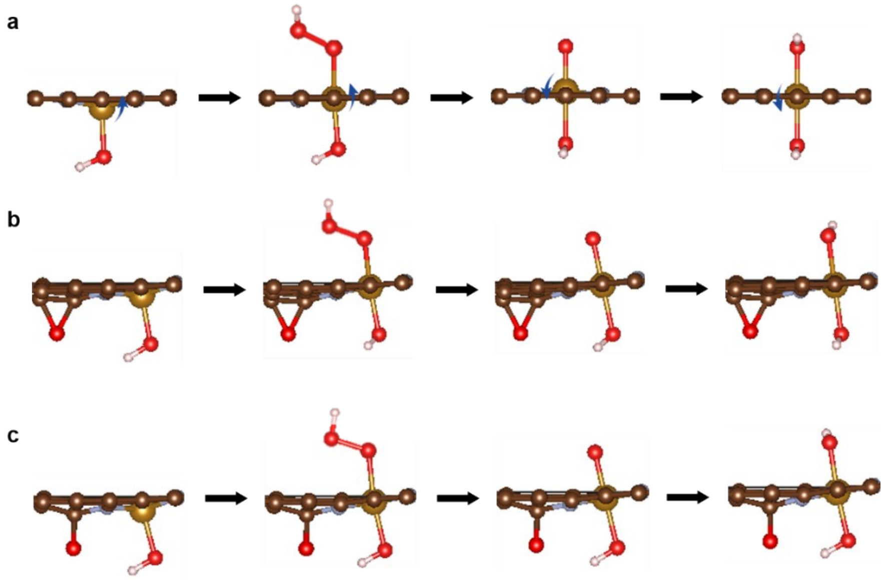

Fig. S26. Side views of the geometries of the clean, Type I and Type II structures with the axial OH ligand. Large Fe displacements are observed in (a) the clean sheet, whereas mild Fe displacements are observed in both (b) Type I and (c) Type II sheets.

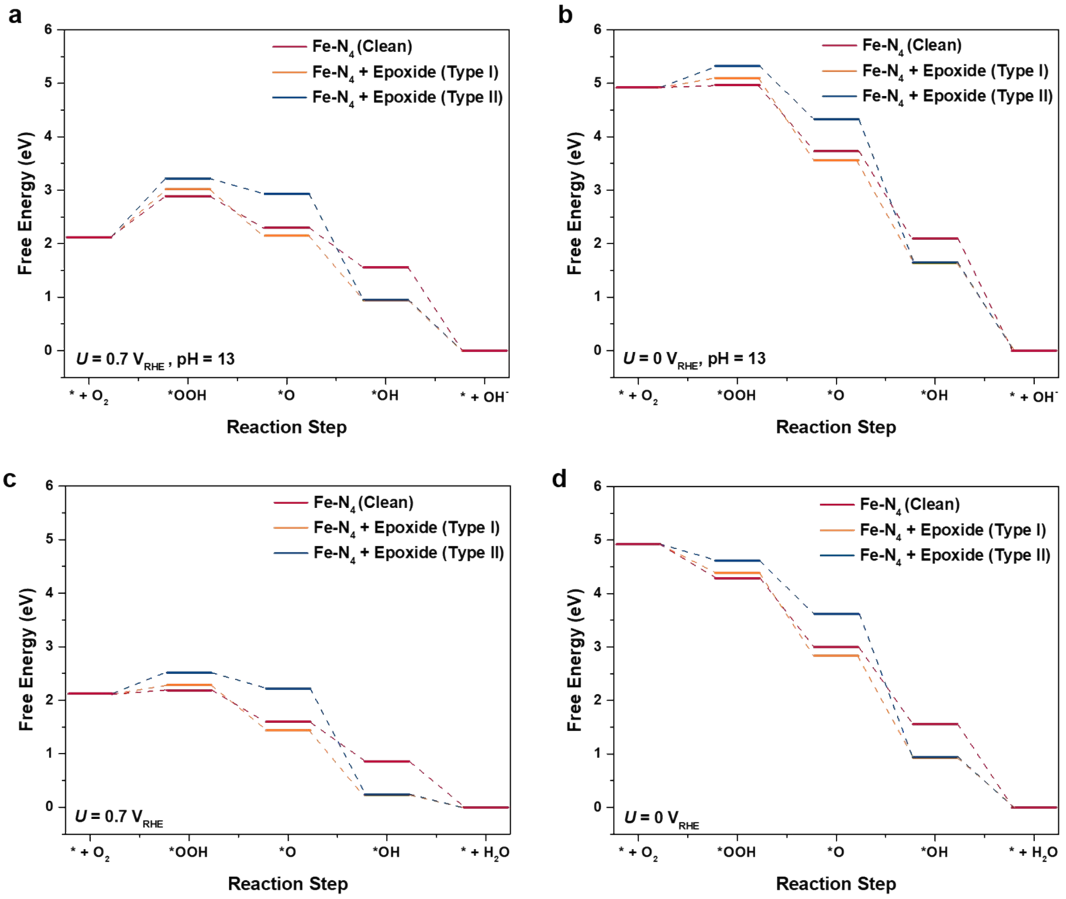

Fig. S27. Free-energy evolution diagrams for ORR on the central Fe atoms at pH = 13 and 1. The clean sheet always shows a more favourable ORR pathway under U = 0.7 V_{RHE} and 0 V_{RHE}, irrespective of the pH.

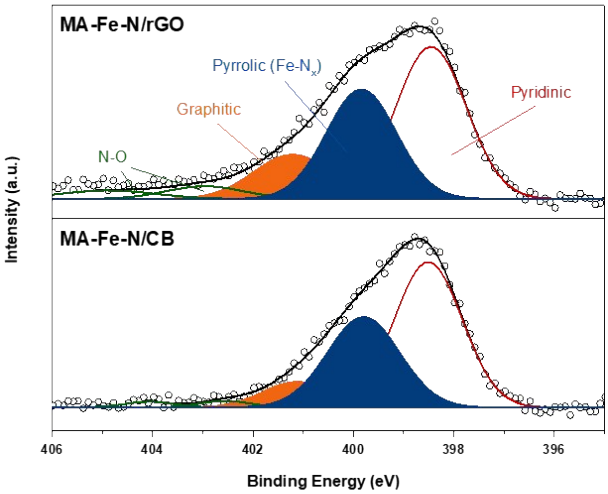

Fig. S28. XPS spectra of N1s deconvolution peaks of MA-Fe-N/rGO and MA-Fe-N/CB catalysts. The pyrrolic-N (Fe-N$_x$) species peaks are much higher than the graphitic-N peaks, implying that numerous FeN$_x$C$_y$ moieties were formed in the MA-Fe-N/rGO and MA-Fe-N/CB catalysts as well.

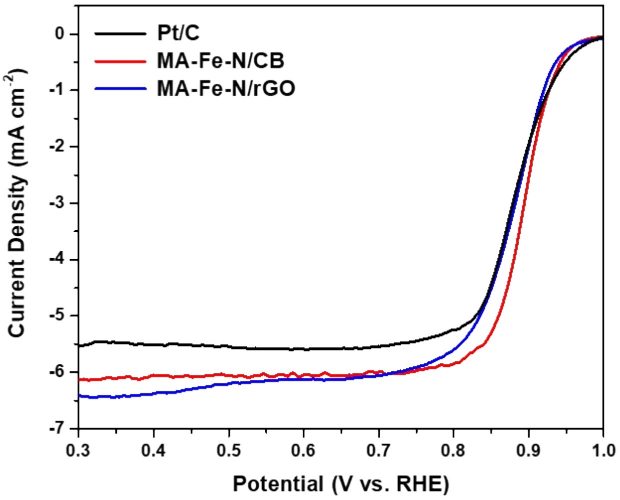

Fig. S29. RDE polarization curves for MA-Fe-N/rGO and MA-Fe-N/CB catalysts in 0.1 M KOH. The current densities at 0.9 V and the half-wave potentials of MA-Fe-N/CB and MA-Fe-N/rGO were 2.54 and 1.97 mA cm^{-2} and 0.89 and 0.88 V$_{RHE}$, respectively. Catalyst loading amount was 0.8 mg cm^{-2} for all measurements (electrode surface area: 0.196 cm^{2}).

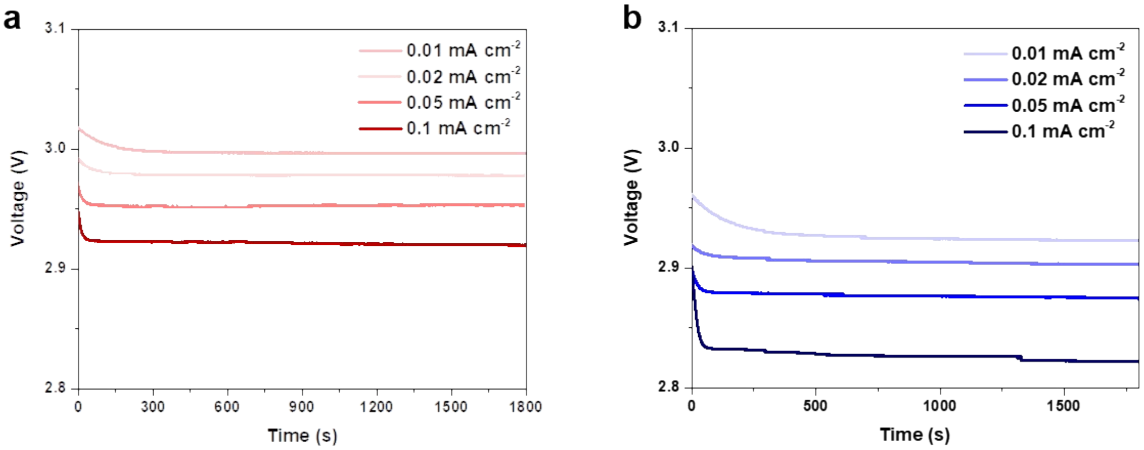

Fig. S30. Rate capability test at different rates ranging from 0.01 to 0.1 mA cm^{-2} for an aqueous Na-air battery. (a) Discharge profiles of MA-Fe-N/CNT loaded air-electrode. (b) Discharge profiles of TA-Fe-N/CNT loaded air-electrode. All chronopotentiometry results were collected after 30 s of equilibration time to exclude side-reaction-derived currents; the loading amount was 2.15 mg cm^{-2}; the electrode surface area was 1 cm^{2}; charging was conducted with the bare carbon felt air-electrode.

Table S1. Raman fitting results of pristine CNT, oxidized CNT, MA-Fe-N/CNT and TA-Fe-N/CNT.

Catalyst	I peak (%)	D peak (%)	D'' peak (%)	G peak (%)	D2 peak (%)	$\text{Area}_D/\text{Area}_G$
Pristine CNT	5.79	32.9	15.1	41.0	5.21	0.80
MA-Fe-N/CNT	12.5	31.6	17.3	31.9	6.7	0.99
TA-Fe-N/CNT	13.4	34.4	18.9	25.3	8.0	1.35
Oxidized CNT	8.49	42.9	10.6	29.6	8.41	1.45

Fitting results were constructed by calculating peak areas; I peak, C-sp^2; D'' peak, distortion, C5 ring or heteroatoms; D2 peak, stretching vibrations in small graphite crystallites covered by O functional groups. Higher portion of the D'' peak and D2 peak in TA-Fe-N/CNT catalyst suggest that onion-like N-doped graphitic shells commonly observed on the Fe-based particles and less reduced carbon structures are obtained.

Table S2. Elemental content of MA-Fe-N/CNT and TA-Fe-N/CNT catalysts, obtained from ICP-OES and elemental analysis measurements.

Sample	Fe (wt%)	C (wt%)	H (wt%)	N (wt%)	O (wt%)
MA-Fe-N/CNT	3.17	88.4	0.38	5.25	2.7
TA-Fe-N/CNT	2.74	89.6	1.94	1.94	4.3

Table S3. Best-fit parameters obtained from the analysis of the Fe *K*-edge EXAFS spectra of MA-Fe-N/CNT and TA-Fe-N/CNT catalysts.

Catalyst	Path	N	R (Å)	σ^2 (Å)	E_0 (eV)	R-factor	R-range	k-range
MA-Fe-N/CNT	$\gamma^{(2)}$-Fe-N	4(0.4)	1.96(1)	0.009(6)	6.531	0.016	1.0 – 3 .3	2.0 – 10 .5
	$\gamma^{(2)}$-Fe-Fe	8(0.7)	2.54(1)	0.01(1)				
	$\gamma^{(2)}$-Fe-C	2(1.2)	2.76(4)	0.002(1)				
	$\gamma^{(3)}$-Fe-C-N	4(1.5)	3.90(5)	0.001(2)				
TA-Fe-N/CNT	$\gamma^{(2)}$-Fe-N	4(0.9)	1.93(2)	0.02(1)	5.486	0.016	1.2 – 3 .4	2.15 – 11 .2
	$\gamma^{(2)}$-Fe-Fe	8(0.6)	2.47(1)	0.005(4)				
	$\gamma^{(2)}$-Fe-C	2(1.0)	3.12(1)	0.01(2)				
	$\gamma^{(3)}$-Fe-C-N	4(1.4)	3.76(7)	0.004(2)				

N, coordination number; *R*, interatomic distance; σ^2, Debye-Waller factor (thermal and structural disorders); E_0, energy shift; *R-factor*, goodness of the fit. The estimated parameter errors are indicated in parentheses. The various paths in the **Table** are generated from the *Feff* calculations of model structure optimized by DFT calculations and Fe foil cif file. The Fe-N, Fe-C and Fe-Fe scattering are the single scattering. The Fe-C-N scattering is the obtuse triangle scattering. The Fourier transformed EXAFS spectra of MA-Fe-N/CNT and TA-Fe-N/CNT catalysts are well reproduced with a combination of these scattering paths. No phase-shift correction was applied to the Fourier transforms. *R-range* and *k-range* are the fitting range for each catalyst.

Table S4. Summary of elemental analysis results for selective microwave-annealed catalysts with different irradiation time, obtained from XPS measurements.

Sample	Pyridinic-N	Pyrrolic-N or Fe-N_x	Graphitic-N	Oxidized N species	Ratio
MA-Fe-N/CNT-3'_w/o AT	60.7	25.2	8.49	5.61	8.49
MA-Fe-N/CNT-4'_w/o AT	55.9	25.0	11.0	8.09	11.0
MA-Fe-N/CNT-5'_w/o AT	57.9	19.6	16.6	5.97	16.6
MA-Fe-N/CNT-6'_w/o AT	50.1	9.53	29.9	10.4	29.9

Table S5. Turnover frequencies ORR based on the CO-titrated sites.

Catalyst	V_m (cm^3 g^{-1})	$MSD_{surface}$ (10^{18}) (site g_{cat}^{-1})	Alkaline Media	Acidic Media
			TOF (0.9 V) (e^- $site^{-1}$ s^{-1})	TOF (0.8 V) (e^- $site^{-1}$ s^{-1})
MA-Fe-N/CNT	0.0677	1.67	5.54	2.19
TA-Fe-N/CNT	0.0542	1.33	1.98	1.02

$MSD_{surface} = n_{CO,\ Catalyst} \times N_A$

Table S6. Comparison of the kinetic parameters of Pt group metal-free catalysts for the ORR in alkaline media.

Catalyst	Half-Wave Potential (V vs. RHE)	Kinetic Current Density @ 0.9V (mA cm^{-2})	Catalyst Loading (mg cm^{-2})	Reference
MA-Fe-N/CNT	**0.92-0.9**	**4.5-3.7**	**0.8-0.2**	***This work***
Fe-SAs/NPS-HC	0.91	4.5	0.4	*6*
pfSAC-Fe	0.91	3.4	0.3	*7*
SA-Fe-HPC	0.89	2.1	0.1	*8*
N-GNR@CNT	0.839	0.9	0.4	*9*
CNT/PC	0.88	2.4	0.8	*10*
FePhen@MOF-ArNH3	0.86	2.1	0.6	*11*
(Fe,Mn)-N-C	0.90	2.7	0.8	*12*
FeCo/C-800	0.82	1.1	0.2	*13*
S/N-Fe$_{27}$	0.87	2.7	0.8	*14*
Fe-N/C-800	0.81	0.6	0.1	*15*
FeCo-OMPC	0.86	1.7	0.6	*16*
FePc-Py-CNT	0.91	3.2	0.3	*17*
NT-G	0.87	2.8	0.5	*18*
Co_3O_4/N-rmGO	0.88	0.2	0.1	*19*

Table S7. Comparison of the kinetic parameters of Pt group metal-free catalysts for the ORR in acid media.

Catalyst	**Half-Wave Potential (V vs. RHE)**	**Kinetic Current Density @ 0.8V (mA cm^{-2})**	**Catalyst Loading (mg cm^{-2})**	**Reference**
MA-Fe-N/CNT	**0.78**	**1.86**	**0.8**	***This work***
Fe-SAs/NPS-HC	0.79	2.0	0.4	*6*
SA-Fe-HPC[b]	0.81	2.3	0.2	8
N-GNR@CNT[a]	0.633	-	0.398	*9*
CNT/PC	0.79	2.6	0.8	10
S/N-Fe_{27}	0.83	3.7[c]	0.8	14
Fe-N/C-800	0.6	-	0.1	*15*
(CM+PANI)-Fe-C[a]	0.8	1.5	0.6	*20*
CNT@Fe-N-PC[a]	0.82	3.6	0.3	*21*
FePhen@MOF-$ArNH_3$	0.78	2.6	0.6	*22*
Fe/N/CF	0.80	3.5	0.4	*23*
PANI-Fe-C[a]	0.8	2.0	0.6	*24*
Fe_3C/C-700	0.71	0.3	0.6	*25*
Fe-N-HCMS[a]	0.68	0.2	0.5	*26*
$Fe_{0.5}$-950[b]	0.90	3.7[c]	0.82	*27*

[a] 0.5M H_2SO_4 [b] 0.1M H_2SO_4 [c] Near limiting current density

Table S8. Bond lengths in the studied model structures *via* DFT calculations.

Model Structure	Adsorbate	Fe-N$_1$	Fe-N$_2$	Fe-N$_3$	Fe-N$_4$
Clean sheet	*	1.981	1.981	1.985	1.985
	*OOH	1.927	1.934	1.927	1.931
	*O	1.981	1.981	1.984	1.985
	*OH	1.924	1.924	1.929	1.930
Type I	*	1.925	1.947	1.926	1.947
	*OOH	1.934	1.944	1.934	1.944
	*O	1.934	1.946	1.934	1.946
	*OH	1.928	1.957	1.931	1.956
Type II	*	1.951	1.939	1.909	1.932
	*OOH	1.942	1.932	1.900	1.939
	*O	1.965	1.944	1.928	1.941
	*OH	1.952	1.941	1.913	1.933

3. Supporting Movie

Movie S1. Preparation of highly reduced carbon-hosted, Fe–N_4 on a CNT via selective microwave annealing (MA-Fe-N/CNT catalyst). This video demonstrates the SMA method. The ternary FePc/CNT@Mel composites were moved into the crucible purged with Ar gas to make the inert atmosphere. Upon microwave irradiation, the CNT support absorbs microwaves and generates heat within dozens of seconds. Then heat migrates to the overall samples and FePc begins to carbonize and immobilize to form Fe–N_4 catalyst on the CNT support.

4. Supporting References

1. G. Kresse, J. Furthmüller, *Comput. Mater. Sci.*, 1996, **6**, 15-50.
2. J. P. Perdew, K. Burke, M. Ernzerhof, *Phys. Rev. Lett.*, 1996, **77**, 3865-3868.
3. T. Bučko, S. Lebègue, J. Hafner, J. G. Ángyán, *Phys. Rev. B***,** 2013, **87**, 064110.
4. J. K. Nørskov, J. Rossmeisl, A. Logadottir, L. Lindqvist, J. R. Kitchin, T. Bligaard, H. Jonsson, *The J. Phys. Chem. B*, 2004, **108**, 17886-17892.
5. I. C. Man, H. -Y. Su, F. Calle-Vallejo, H. A. Hansen, J. I. Martínez, N. G. Inoglu, J. Kitchin, T. F. Jaramillo, J. K. Nørskov, J. Rossmeisl, *Chem. Cat. Chem.*, 2011, 3, 1159-1165.
6. Y. Chen, S. Ji, S. Zhao, W. Chen, J. Dong, W. -C. Cheong, R. Shen, X. Wen, L. Zheng, A. I. Rykov, S. Cai, H. Tang, Z. Zhuang, C. Chen, Q. Peng, D. Wang, Y. Li, *Nat. Commun.*, 2018, **9**, 5422.
7. P. Peng, L. Shi, F. Huo, C. Mi, X. Wu, S. Zhang, Z. Xiang, *Sci. Adv.*, 2019, **5**, eaaw2322.
8. Z. Zhang, J. Sun, F. Wang, L. Dai, *Angew. Chem. Int. Ed.*, 2018, **57**, 9038-9043.
9. L. Xue, Y. Li, X. Liu, J. Shang, H. Duan, L. Dai, J. Shui, *Nat. Commun.*, 2018, **9**, 3819.
10. Y. J. Sa, D. -H. Seo, J. Woo, J. T. Lim, J. Y. Cheon, S. Y. Yang, J. M. Lee, D. Kang, T. J. Shin, H. S. Shin, H. Y. Jeong, C. S. Kim, M. G. Kim, T. -Y. Kim, S. H. Joo*, J. Am. Chem. Soc.*, 2016, **138**, 15046-15056.
11. K. Strickland, E. Miner, Q. Jia, U. Tylus, N. Ramaswamy, W. Liang, M. -T. Sougrati, F. Jaouen, S. Mukerjee, *Nat. Commun.*, 2015, **6**, 7343.
12. N. R. Sahraie, U. I. Kramm, J. Steinberg, Y. Zhang, A. Thomas, T. Reier, J. -P. Paraknowitsch, P. Strasser, *Nat. Commun.*, 2015, **6**, 8618.
13. Q. Lin, X. Bu, A. Kong, C. Mao, F. Bu, P. Feng, *Adv. Mater.*, 2015, **27**, 3431-3436.
14. N. R. Sahraie, J. P. Paraknowitsch, C. Göbel, A. Thomas, P. Strasser, *J. Am. Chem. Soc.*, 2014, **136**, 14486-14497.
15. L. Lin, Q. Zhu, A. -W. Xu, *J. Am. Chem. Soc.*, 2014, **136**, 11027-11033.
16. J. Y. Cheon, T. Kim, Y. Choi, H. Y. Jeong, M. G. Kim, Y. J. Sa, J. Kim, Z. Lee, T. -H. Yang, K. Kwon, O. Terasaki, G. -G. Park, R. R. Adzic, S. H. Joo, *Sci. Rep.*, 2013, **3**, 2715.
17. R. Cao, R. Thapa, H. Kim, X. Xu, M. G. Kim, Q. Li, N. Park, M. Liu, J. Cho, *Nat. Commun.*, 2013, **4**, 2076.
18. Y. Li, W. Zhou, H. Wang, L. Xie, Y. Liang, F. Wei, J. -C. Idrobo, S. J. Pennycook, H. Dai, *Nat. Nanotechnol.*, 2012, **7**, 394-400.
19. Y. Liang, Y. Li, H. Wang, J. Zhou, T. Regier, H. Dai, *Nat. Mater.*, 2011, **10**, 780-786.
20. H. T. Chung, D. A. Cullen, D. Higgins, B. T. Sneed, E. F. Holby, K. L. More, P. Zelenay, *Science*, 2017, **357**, 479-484.
21. J. -C. Li, Z.-Q. Yang, D. -M. Tang, L. Zhang, P. -X. Hou, S. -Y. Chao, C. Liu, M. Cheong, G. -X. Li, F. Zhang, H. -M. Cheng, *NPG Asia Mater.*, 2018, **10**, e461.

22. J. Li, S. Ghoshal, W. Liang, M. -T. Sougrati, F. Jaouen, B. Halevi, S. McKinney, G. McCool, C. Ma, X. Yuan, Z. -F. Ma, S. Mukerjee, Q. Jia, *Energy Environ. Sci.*, 2016, **9**, 418-2432.
23. J. Shui, C. Chen, L. Grabstanowicz, D. Zhao, D. -J. Liu, *Proc. Natl. Acad. Sci.*, 2015, 112, 10629-10634.
24. 24 G. Wu, K. L. More, C. M. Johnston, P. Zelenay, *Science*, 2011, **3323**, 443-447.
25. Y. Hu, J. O. Jensen, W. Zhang, L. N. Cleemann, W. Xing, N. J. Bjerrum, Q. Li, *Angew. Chem. Int. Ed.*, 2014, **53**, 3675-3679.
26. M. Zhou, C. Yang, K. -Y. Chan, *Adv. Energy Mater.*, 2014, **4**, 1400840.
27. A. Zitolo, V. Goellner, V. Armel, M. -T. Sougrati, T. Mineva, L. Stievano, E. Fonda, F. Jaouen, *Nat. Mater.*, 2015, **14**, 937-942.